



Anion exchange strategy for construction of sesame-biscuit-like $\text{Bi}_2\text{O}_2\text{CO}_3/\text{Bi}_2\text{MoO}_6$ nanocomposites with enhanced photocatalytic activity

Yang-Sen Xu, Wei-De Zhang*

School of Chemistry and Chemical Engineering, South China University of Technology, 381 Wushan Road, Guangzhou 510640, People's Republic of China



ARTICLE INFO

Article history:

Received 24 January 2013

Received in revised form 2 April 2013

Accepted 7 April 2013

Available online 13 April 2013

Keywords:

Heterostructure

$\text{Bi}_2\text{O}_2\text{CO}_3$

Bi_2MoO_6

Hydrothermal synthesis

Anion exchange

Photocatalysis

ABSTRACT

Heterostructured sesame-biscuit-like $\text{Bi}_2\text{O}_2\text{CO}_3/\text{Bi}_2\text{MoO}_6$ nanocomposites were successfully prepared via a facile anion exchange approach under hydrothermal process with the graphitic carbon nitride ($\text{g-C}_3\text{N}_4$) as the precursor of carbonate anion. The $\text{Bi}_2\text{O}_2\text{CO}_3/\text{Bi}_2\text{MoO}_6$ nanocomposites are based on ca. 30–45 nm thick single-crystal Bi_2MoO_6 nanoplatelets embedded with homogeneously dispersed $\text{Bi}_2\text{O}_2\text{CO}_3$ nanoparticles (less than 10 nm). The intimate interfacial contact between the $\text{Bi}_2\text{O}_2\text{CO}_3$ nanoparticles and the Bi_2MoO_6 nanoplatelets endows the nanocomposite catalysts with high visible light photocatalytic activity for the degradation of rhodamine B. The photocatalyst prepared with 11 wt% $\text{g-C}_3\text{N}_4$ as the precursor shows the highest activity, which can degrade 99% rhodamine B in 30 min. The degradation rate of the $\text{Bi}_2\text{O}_2\text{CO}_3/\text{Bi}_2\text{MoO}_6$ photocatalyst is more than 64 times faster than that of using bare Bi_2MoO_6 under visible light irradiation. The dramatically enhanced photocatalytic activity of the $\text{Bi}_2\text{O}_2\text{CO}_3/\text{Bi}_2\text{MoO}_6$ photocatalysts can be attributed to the large heterojunction interface, intrinsically layered structure, two-dimensional morphology and effective separation of the photoinduced carriers at the interfaces and in the semiconductors. In addition, the $\text{Bi}_2\text{O}_2\text{CO}_3/\text{Bi}_2\text{MoO}_6$ catalyst is highly stable during the reaction and can be used repeatedly. These features suggest the current heterostructured photocatalysts can be applied in environmental remediation and waste water treatment. This method may usher a new phase for the synthesis of novel and highly efficient $\text{Bi}_2\text{O}_2\text{CO}_3$ -based heterostructures for light-harvesting and energy conversion applications.

© 2013 Elsevier B.V. All rights reserved.

1. Introduction

Metal oxide semiconductors are promising photocatalysts for a plenty of applications, especially in the area of energy conversion and environment treatment, including splitting of water, dye-sensitized solar cells, oxidation of pollutants and even anti-fogging/anti-microbial coating for windows and lenses [1–3]. TiO_2 , the key photocatalyst for convenient wastewater treatment and other essential cleaning processes, however, suffers from such problems as ineffective sunlight capture and conversion. In recent years, the development of efficient visible-light-active photocatalysts has become a buzzword in photocatalysis [2,4–6].

Given the low price and abundant source on Earth, the bismuth-containing semiconductors have been attracting extensive attention these days [7–10]. BiOCl , with bandgap ranging from 3.1 eV to 3.5 eV, is an Aurivillius-layered structure with $[\text{Bi}_2\text{O}_2]^{2+}$ slabs interleaved by double slabs of Cl in the tetragonal structure [11]. $\text{Bi}_2\text{O}_2\text{CO}_3$ is another semiconductor with large bandgap

(3.3 eV) [12], which also belongs to the layered Aurivillius-related oxide family, and has long since been used for medical and healthcare purposes [13]. However, both BiOCl and $\text{Bi}_2\text{O}_2\text{CO}_3$ can absorb only UV light (less than 5% of the solar light). On the other hand, Bi_2MoO_6 is a smaller bandgap (2.5–2.8 eV) semiconductor which can capture visible light ($420 \leq \lambda \leq 500 \text{ nm}$) of the omnipresent sunlight and is a well-known photocatalyst for water splitting and degradation of organic dyes [14,15]. Regrettably, the overall efficiency of individual phase Bi_2MoO_6 is low because of the rapid recombination of electron–hole (e^- – h^+) pairs after excitation. Actually, isolated component usually is no longer sufficient to cope with technological challenges involved in the development of an environmentally benign energy infrastructure [1]. To overcome the intrinsic limitations of single metal oxide, several significant accomplishments have already been demonstrated on the component level, in which coupling a semiconductor with another with matching energetic levels of valence band (VB) and conduction band (CB) is the most frequently applied strategy [16]. In particular, the embedded-junction fashion can harness most of the solar spectrum, generating rather high solar-conversion efficiency, as being demonstrated in the p-GaInP₂/GaAs junction [17]. However, manufacturing cost and material stability restrain

* Corresponding author. Tel.: +86 20 8711 4099; fax: +86 20 8711 4099.

E-mail address: zhangwd@scut.edu.cn (W.-D. Zhang).

it from being widely used. The catalysts with triple junctions that mimic the direct solar-to-fuels conversion has shown the prospect, especially with the recent demonstration of incorporating low-cost, earth-abundant catalysts for the utilization of sunlight [18]. For example, such bismuth-based catalysts as heterojunctioned $\text{BiOCl}_{1-x}\text{Br}_x$ exhibit a stronger photocatalytic activity than BiOCl and BiOBr , with the activity reaching the maximum at $x = 0.5$ [19]. In addition, the solid solutions $\text{BiOCl}_{1-x}\text{I}_x$ ($x = 0.2\text{--}1.0$) have bandgap in the range between 1.92 eV and 2.31 eV, which can absorb visible light intensely and exhibit high photocatalytic activity under visible light for the degradation of methyl orange (MO) and rhodamine B (RhB) [20]. The causes for the high photocatalytic activity of the BiOCl/BiOI and $\text{BiOCl}/\text{BiOBr}$ are believed to be the heterojunction structure and the internal electric field between each $[\text{Bi}_2\text{O}_2]^{2+}$ cation layer and its adjacent X^- halide layers [19]. Analogously, $\text{Bi}_2\text{O}_2\text{CO}_3/\text{BiOI}$ heterojunction shows enhanced visible-light photocatalytic activity in photocleaning of wastewater containing RhB, methylene blue (MB) and crystal violet [21]. Bi_2MoO_6 -based heterostructure has also drawn great attention for its excellent visible light harvesting ability [22–24]. Solid solutions of $\text{Bi}_2\text{Mo}_x\text{W}_{1-x}\text{O}_6$ nanoplatelets with adjustable bandgap exhibit enhanced visible-light photocatalytic activity for the photodecomposition of MB [25]. Heterostructured $\text{Bi}_{3.64}\text{Mo}_{0.36}\text{O}_{6.55}/\text{Bi}_2\text{MoO}_6$ catalyst shows notably enhanced photocatalytic activity toward the degradation of RhB and phenol under visible light irradiation, and even mineralize organic compounds to CO_2 efficiently [26]. Most importantly, the interfaces between these heterojunction composites (heterointerfaces), with unusual charge states that are inaccessible in bulk materials can lead to nontrivial local atomic and electronic structure, owing to the presence of dangling bonds and incomplete atomic coordination [27,28]. This phenomenon has been demonstrated in the $\text{LaAlO}_3/\text{SrTiO}_3$ system, which is composed of two insulators but shows a surprising conductive behavior due to the extremely high mobility of a two-dimensional (2D) electron gas at the heterointerface [29]. Additionally, BiOCl , $\text{Bi}_2\text{O}_2\text{CO}_3$ and Bi_2MoO_6 belong to the layered Aurivillius-related oxide family, consisting of $[\text{Bi}_2\text{O}_2]^{2+}$ layers ($\text{X}-\text{Bi}-\text{O}-\text{Bi}-\text{X}$) sandwiched between two slabs of X ions, atoms or groups (where $\text{X} = \text{Cl}^-$, CO_3^{2-} and MoO_4^{2-}). They can easily grow together to form heterostructures with morphology and component being controlled by tuning the ratio of CO_3^{2-} and MoO_4^{2-} .

Herein, we report one-pot hydrothermal strategy for controlled synthesis of sesame-biscuit-like $\text{Bi}_2\text{O}_2\text{CO}_3/\text{Bi}_2\text{MoO}_6$ heterostructured photocatalysts from BiOCl via anion exchange. The content of $\text{Bi}_2\text{O}_2\text{CO}_3$ in the composites was regulated in a sophisticated manner by modulating the amount of $\text{g-C}_3\text{N}_4$ as a raw material, which was decomposed to generate CO_3^{2-} in the hydrothermal process. The $\text{Bi}_2\text{O}_2\text{CO}_3/\text{Bi}_2\text{MoO}_6$ composites exhibit much higher photocatalytic activity than the single phase Bi_2MoO_6 or $\text{Bi}_2\text{O}_2\text{CO}_3$ toward the degradation of RhB under visible light illumination. The evolution of structure and the photocatalytic enhancement mechanism are thoroughly discussed. The results demonstrate that the combination of the two semiconductors in such a way as sesame-biscuit-like heterostructure can be a promising approach to greatly improve the photocatalytic performance. This method may be further extended to synthesize novel and highly efficient visible-light-driven $\text{Bi}_2\text{O}_2\text{CO}_3$ -based heterojunction photocatalysts.

2. Experimental

2.1. Chemicals

Sodium hydroxide (NaOH), hydrochloric acid (HCl), sodium molybdate ($\text{Na}_2\text{MoO}_4 \cdot 2\text{H}_2\text{O}$) and bismuth nitrate ($\text{Bi}(\text{NO}_3)_3 \cdot 5\text{H}_2\text{O}$) were purchased from Sinopharm Chemical Reagent Co., Ltd. All

chemicals were used without further purification. Deionized water was used throughout this study. $\text{g-C}_3\text{N}_4$ was prepared according to a previous report [30].

2.2. Synthesis of $\text{Bi}_2\text{O}_2\text{CO}_3/\text{Bi}_2\text{MoO}_6$ heterostructure

$\text{Bi}_2\text{O}_2\text{CO}_3/\text{Bi}_2\text{MoO}_6$ composites were synthesized by a hydrothermal method. In brief, 0.80 g $\text{Bi}(\text{NO}_3)_3 \cdot 5\text{H}_2\text{O}$ was dispersed in 20 mL 0.02 M HCl under ultrasonic treatment for 10 min, then $\text{g-C}_3\text{N}_4$ was added into the above suspension. After 30 min ultrasonication, 0.20 g $\text{Na}_2\text{MoO}_4 \cdot 2\text{H}_2\text{O}$ was added. The pH value was adjusted to 7.0–8.0 by using 1.0 M NaOH. After stirring for 10 min, the mixture was transferred into a Teflon-lined autoclave up to 80% of the total volume. Then, the sealed autoclave was heated at 180 °C for 12 h. After being cooled down to room temperature naturally, the products were collected by filtration and washed by deionized water and dried at 60 °C for 12 h.

2.3. Characterization

The crystal structures and phase compositions of the prepared samples were determined by powder X-ray diffractometer (X'Pert PRO MPD). The size and surface morphology of the samples were observed through a scanning electron microscope (SEM, LEO 1530 VP) and transmission electron microscope (TEM, Tecnai G220, FEI). UV–vis diffuse reflection spectra (DRS) of the samples were recorded using a UV-vis spectrophotometer (UV-3010, Hitachi, Japan) by using BaSO_4 as a reference. The BET specific surface area was measured using a Quantochrome NOVA 1200e instrument at 77 K. The X-ray photoelectron spectroscopy (XPS, Axis Ultra DLD, Kratos) analysis was carried out with a monochromatized Al K α X-ray source (15 kV, 200 W), and C1s (284.6 eV) was used to calibrate the peak positions. Electron spin resonance (ESR) spectra of paramagnetic species spin-trapped with DMPO were recorded with a Bruker ER200D-SRC-1012 spectrometer. ICP-AES measurements were performed using an ICP spectrometer (Prodigy, Teledyne Lee-man Labs, USA).

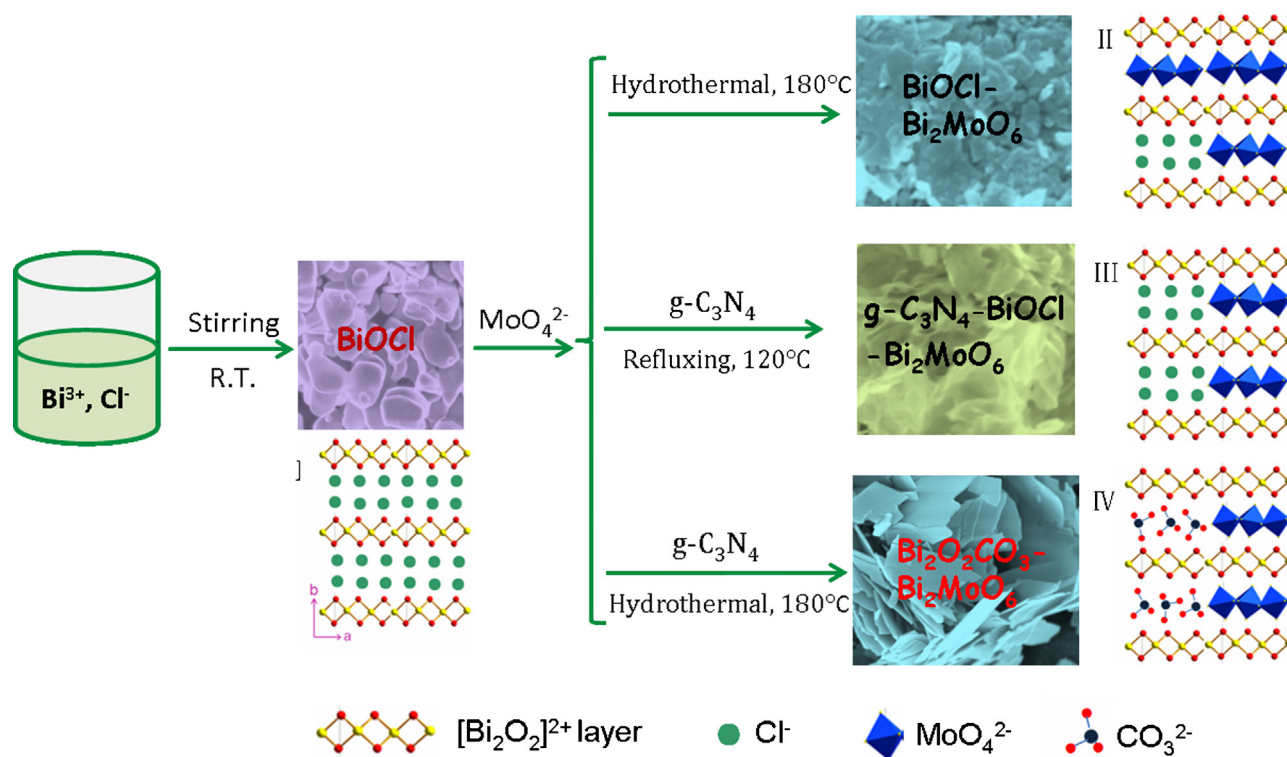
2.4. Measurement of photocatalytic activity

The photocatalytic performance of the prepared products was evaluated by degradation of RhB under visible light irradiation at room temperature. A 300 W tungsten halide lamp (Foshan Electric Light Ltd.) was used as light source and equipped with an ultraviolet cutoff filter to provide visible light ($\lambda \geq 420$ nm). The distance between the liquid surface of the suspension and the light source was set about 20 cm. For each run, 0.10 g photocatalyst was added into 100 mL RhB solution (5.0 mg/L). Prior to irradiation, the suspension was stirred in the dark for 30 min to ensure the absorption–desorption equilibrium of the dye on the catalyst. During the absorption and irradiation process, at time intervals of 10 min, approximately 3 mL of suspension was collected, then centrifuged at 12,000 rpm for 3 min and analyzed by a Hitachi U-3900H Spectrophotometer.

3. Results and discussion

3.1. Crystal structure and morphology

The synthesis process of the heterostructured photocatalysts was schematically illustrated in Scheme 1. It is noted that every plane of atoms in II–IV parallel to the junction is on the whole neutrally corresponding to a nonpolar junction [31]. In order to overcome the kinetic barrier, high solvation energy usually is required in anion exchange reactions. In this case, the $\text{Bi}_2\text{O}_2\text{CO}_3/\text{Bi}_2\text{MoO}_6$ nanoplatelets were prepared through anion



Scheme 1. Schematic illustration of the synthesis process of Bi_2MoO_6 -based nanocomposites via anion exchange strategy.

exchange reaction from BiOCl platelets under hydrothermal treatment at 180°C for 12 h. In such a process, CO_3^{2-} was generated from the decomposition of $\text{g-C}_3\text{N}_4$. The evolution of the phase structure of the obtained products was carried out based on the temperature-dependent experiments, and the structure of the prepared samples was characterized by XRD, as shown in Fig. 1. The BiOCl platelets with exposed (001) facets were easily obtained at room temperature by stirring $\text{Bi}(\text{NO}_3)_3 \cdot 5\text{H}_2\text{O}$ in 0.02 M HCl . As indicated in Fig. 1b, the obtained BiOCl is tetragonal (JCPDS 06-249), and the (001), (002) and (003) diffraction peaks are sharper and stronger while (110) is relatively weaker. This means that the BiOCl favors to grow along the c axis ([001] orientations) [11]. This orientated growth arises from the strong absorption of H^+ on the (001) facet of BiOCl , which terminates with a high density of oxygen atom [32,33]. After adding $\text{Na}_2\text{MoO}_4 \cdot 2\text{H}_2\text{O}$ and adjusting the pH of the solution to 7, the peaks of BiOCl weakened but no new Bi_2MoO_6 diffraction peak appeared (shown in Fig. 1c), which confirms that such anion exchange reaction cannot be achieved at room temperature. Under hydrothermal treatment at 180°C , a well crystallized orthorhombic structure of Bi_2MoO_6 ($a = 5.506 \text{ \AA}$, $b = 16.226 \text{ \AA}$, $c = 5.487 \text{ \AA}$, JCPDS 72-1425) was formed (Fig. 1d), although BiOCl still existed in the composite. After 11 wt% $\text{g-C}_3\text{N}_4$ was introduced into the reaction system, a hybrid composed of $\text{g-C}_3\text{N}_4$, BiOCl and Bi_2MoO_6 was found by refluxing at 120°C for 12 h, as illustrated in Fig. 1e. However, this precursor can easily transfer to $\text{Bi}_2\text{O}_2\text{CO}_3/\text{Bi}_2\text{MoO}_6$ composite at 180°C under hydrothermal treatment. As vividly shown in Fig. 1f, some diffraction peaks of tetragonal $\text{Bi}_2\text{O}_2\text{CO}_3$ ($a = 3.865 \text{ \AA}$, $b = 3.865 \text{ \AA}$, $c = 13.675 \text{ \AA}$, JCPDS 41-1488) appeared and no BiOCl phase was detected by the XRD analysis, which means that $\text{Bi}_2\text{O}_2\text{CO}_3/\text{Bi}_2\text{MoO}_6$ composite was obtained. The absence of Cl^- and the presence of CO_3^{2-} in the sample can be further confirmed by XPS (Fig. S1) and FT-IR (Fig. S2) spectra. These results obviously indicate that Cl^- in BiOCl indeed exchanged with CO_3^{2-} and MoO_4^{2-} at 180°C under hydrothermal condition.

In addition, a time-dependent experiment was carried out at 180°C and the XRD patterns of the obtained samples are displayed in Fig. 2. After reacting at 180°C for 2 h, Bi_2MoO_6 peaks appeared besides those of the BiOCl (in Fig. 2a). As the reaction time prolonged to 6 h, the intensity of the diffraction peaks of BiOCl declined gradually while the intensity of the diffraction peaks of Bi_2MoO_6 and $\text{Bi}_2\text{O}_2\text{CO}_3$ rose, especially the peaks of (013) and (002) of $\text{Bi}_2\text{O}_2\text{CO}_3$ (Fig. 2b and c). After 8 h reaction, no BiOCl was distinguished in the composite (in Fig. 2d), which is in agreement with the XPS analysis, by which no Cl was detected in the sample (Fig. S1). A composite of Bi_2MoO_6 and $\text{Bi}_2\text{O}_2\text{CO}_3$ with fine crystal structure was formed after 12 h reaction (Fig. 2e). Moreover, it is found that the crystal structure plays an important role in determining the final morphology of the products. The layered crystal structure containing $[\text{Bi}_2\text{O}_2]^{2+}$ slabs enables the chemical transformation from BiOCl platelets to Bi_2MoO_6 and $\text{Bi}_2\text{O}_2\text{CO}_3$ with high fidelity and the products maintain the platelet morphology.

The morphology of the products was further characterized by SEM, TEM, and HRTEM. As displayed in Fig. 3A, one can obviously observe that BiOCl nanoplatelets are obtained (Scheme 1(I)). $\text{g-C}_3\text{N}_4/\text{BiOCl}/\text{Bi}_2\text{MoO}_6$ hybrid (Scheme 1(III)) obtained by refluxing at 120°C with ultrathin sheet-like buildings can be observed in Figs. 3B and S3. However, the $\text{BiOCl}/\text{Bi}_2\text{MoO}_6$ hybrid (Fig. 3C and Scheme 1(II)) shows an irregular morphology with length ranging from 200 nm to $1 \mu\text{m}$. The $\text{Bi}_2\text{O}_2\text{CO}_3/\text{Bi}_2\text{MoO}_6$ obtained in hydrothermal process with adding 11 wt% $\text{g-C}_3\text{N}_4$ demonstrates nanoplatelet feature, as shown in Fig. 3D and Scheme 1(IV). The close-up view of the nanoplatelets presented in Fig. 3E indicates that the nanoplatelets are ca. 30–45 nm in thickness and about 200 nm– $1 \mu\text{m}$ in length. The white arrows in Fig. 3E suggest the lamellar nanoplatelets are spontaneously rolled into curly structures driven by excess surface energy [34]. Actually, the layered nature favors the self-assembly of the units to form the characteristic platelet-like nanostructure of the materials. Furthermore, the similarly layered structure of the BiOCl , $\text{Bi}_2\text{O}_2\text{CO}_3$ and

Table 1
Physicochemical properties of the Bi_2MoO_6 -based composites.

Samples	T ($^{\circ}\text{C}$)	Method	Morphology	S_{BET} (m^2g^{-1}) ^c	λ (nm) ^d	K (min^{-1}) ^e
BiOCl^{a}	25	Stirring	Nanoplatelets	4.8	376	–
$\text{g-C}_3\text{N}_4/\text{BiOCl}$	25	Stirring	Nanoplatelets	–	455	–
$\text{g-C}_3\text{N}_4/\text{BiOCl}/\text{Bi}_2\text{MoO}_6$	120	Refluxing	Nanoflowers	22.8	483	–
$\text{BiOCl}/\text{Bi}_2\text{O}_2\text{CO}_3/\text{Bi}_2\text{MoO}_6$	150	Hydrothermal	Nanoplatelets	–	480	–
$\text{Bi}_2\text{O}_2\text{CO}_3/\text{Bi}_2\text{MoO}_6$	170	Hydrothermal	Nanoplatelets	15.6	485	0.1109
$\text{BiOCl}/\text{Bi}_2\text{O}_2\text{CO}_3/\text{Bi}_2\text{MoO}_6$	180 ^b	Hydrothermal	Nanoplatelets	–	≤ 480	–
$\text{Bi}_2\text{O}_2\text{CO}_3/\text{Bi}_2\text{MoO}_6$	180	Hydrothermal	Nanoplatelets	14.2	485	0.1305
$\text{Bi}_2\text{O}_2\text{CO}_3$	160	Hydrothermal	Nanoplatelets	5.4	377	0.0003
Bi_2MoO_6	180	Hydrothermal	Nanoplatelets	6.2	526	0.0073

^a The starting materials are $\text{Bi}(\text{NO}_3)_3 \cdot 5\text{H}_2\text{O}$ and HCl , while the rest are $\text{Bi}(\text{NO}_3)_3 \cdot 5\text{H}_2\text{O}$, $\text{g-C}_3\text{N}_4$, HCl and $\text{Na}_2\text{MoO}_4 \cdot 2\text{H}_2\text{O}$.

^b The reaction time is 6 h, while the rest are 12 h.

^c BET surface area.

^d The end of absorbed wavelength in DRS spectra.

^e The apparent reaction rate constant (k) of RhB photodegradation, which is calculated based on a pseudo-first-order kinetic model. No results are shown for the BiOCl -based composite because of photo-sensitization effect.

Bi_2MoO_6 is favorable for the anion exchange and the formation of the $\text{Bi}_2\text{O}_2\text{CO}_3/\text{Bi}_2\text{MoO}_6$. Fig. 3F shows the obtained $\text{Bi}_2\text{O}_2\text{CO}_3$ nanoplatelets. The physicochemical properties of the Bi_2MoO_6 -based composites are listed in Table 1.

More detailed structural information of the as-synthesized composite is provided by TEM analysis. The heterostructure of the

$\text{Bi}_2\text{O}_2\text{CO}_3/\text{Bi}_2\text{MoO}_6$ nanoplatelets obtained with adding 11 wt% $\text{g-C}_3\text{N}_4$ in the starting materials was characterized. The semi-transparent and wrinkled features in Fig. 4A vividly illustrate the well-defined platelet-shaped nanostructure of $\text{Bi}_2\text{O}_2\text{CO}_3/\text{Bi}_2\text{MoO}_6$ composite, which also shows that most nanoplatelets are rectangles with lengths of 500 nm–1 μm and widths of 100–600 nm,

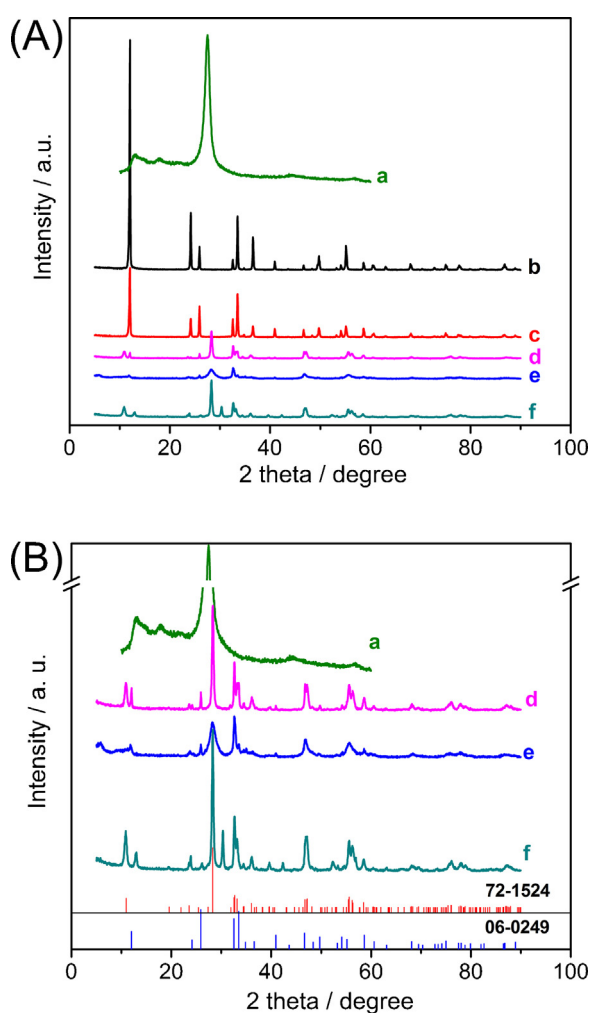


Fig. 1. (A) XRD patterns of pure $\text{g-C}_3\text{N}_4$ (a), pure BiOCl obtained at room temperature before (b) and after (c) $\text{Na}_2\text{MoO}_4 \cdot 2\text{H}_2\text{O}$ was added; $\text{BiOCl}/\text{Bi}_2\text{MoO}_6$ synthesized at 180°C by hydrothermal method without $\text{g-C}_3\text{N}_4$ (d); samples prepared with 11 wt% $\text{g-C}_3\text{N}_4$ by refluxing process at 120°C (e) and hydrothermal method at 180°C (f). (B) A magnified view of (d–f) in (A).

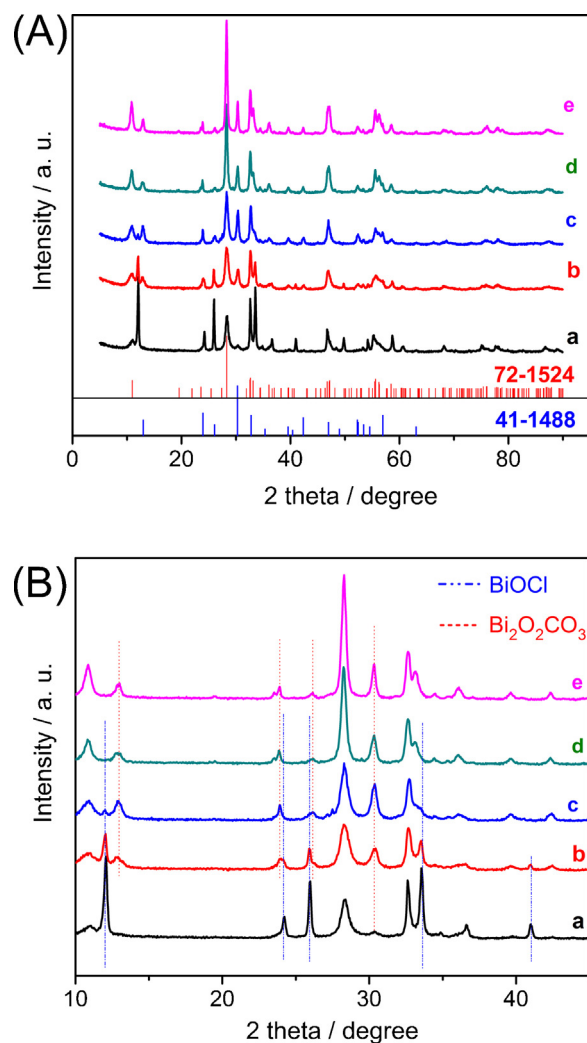


Fig. 2. (A) XRD patterns of the Bi_2MoO_6 -based nanocomposites prepared by hydrothermal process at 180°C in the presence of 11 wt% $\text{g-C}_3\text{N}_4$, (a) 2 h, (b) 4 h, (c) 6 h, (d) 8 h and (e) 12 h. (B) An enlarged view of (A) with the 2θ between 10° and 45° .

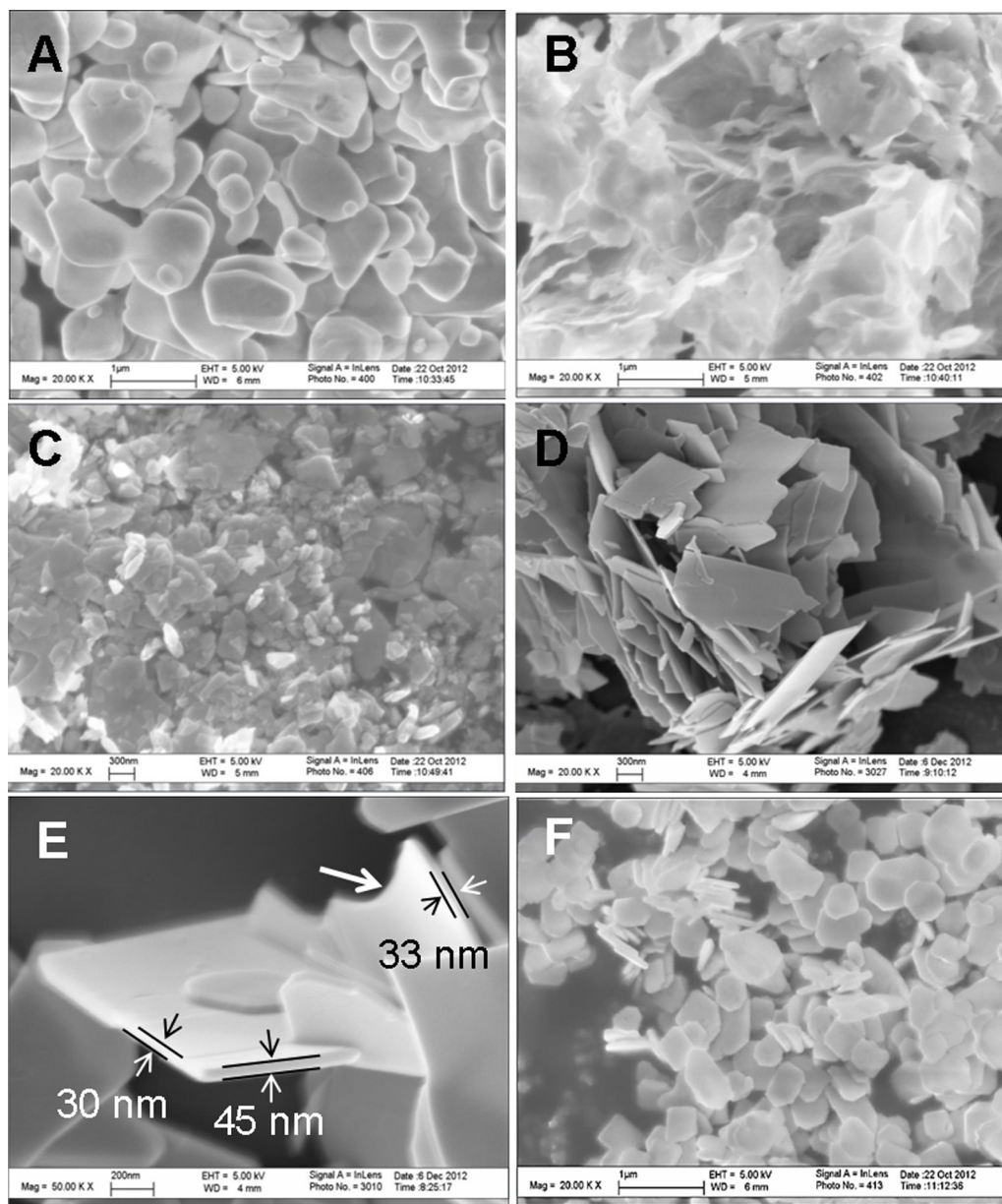


Fig. 3. SEM images of the BiOCl (A), g-C₃N₄/BiOCl/Bi₂MoO₆ (B), BiOCl/Bi₂MoO₆ (without addition of g-C₃N₄) (C), Bi₂O₂CO₃/Bi₂MoO₆ (11 wt% g-C₃N₄ added) of low (D) and high magnification (E) and Bi₂O₂CO₃ (F).

which is consistent with the SEM observations in Fig. 3D and E. Higher magnification TEM images (Fig. 4B and C) provide the detailed morphology of the Bi₂O₂CO₃/Bi₂MoO₆ nanoplatelets, which reveals that many nanoparticles with size smaller than 10 nm are homogeneously dispersed and embedded in the 30–45 nm thick two-dimensional nanoplatelet matrix. The typical HRTEM images, as shown in Fig. 4D and E, further demonstrate the detailed nanojunction structure. Obviously, the lattice fringes and the interface of Bi₂O₂CO₃ and Bi₂MoO₆ can be observed. The measured d-spacings of the crystallographic planes are about 0.688 and 0.341 nm, which correspond well to the (002) and (004) planes of tetragonal Bi₂O₂CO₃ respectively. This observation reveals a preferred in-plane (001) orientation of the layer-structured Bi₂O₂CO₃. Importantly, the dominantly exposed facet of the Bi₂MoO₆ can be identified as (200) plane with the measured spacing between the adjacent fringes of 0.277 nm. In the magnified image, as the white line marks in Fig. 4F, the crystal lattice defect of Bi₂O₂CO₃

at the interface of the composite is also observed. The results suggest that nanoparticles of Bi₂O₂CO₃ are interlaced in the Bi₂MoO₆ nanoplatelet matrix, forming a sesame-biscuit-like structure of Bi₂O₂CO₃/Bi₂MoO₆ nanocomposite.

Fig. 5 displays the selected area electron diffraction (SAED) of Bi₂MoO₆ and Bi₂O₂CO₃/Bi₂MoO₆ composite. The set of diffraction spots in Fig. 5A can be indexed to orthorhombic Bi₂MoO₆ on the [010] projection, indicating the single-crystalline nature of the nanoplatelet, which agrees well with the observation of HRTEM in Fig. 4D and E. Furthermore, some weak diffraction spots can also be found at the forbidden sites (such as (100) and (102)), as indicated by white arrows in Fig. 5A. These weak diffraction spots can be assigned to the high-order Laue zone caused by the combined effects of elongation of the diffraction spots along the normal of the nanoplatelet and narrowed Laue zone along the [010] direction (the ultralarge {010} spacing, 1.619 nm) [25]. The SAED of the interface of the Bi₂O₂CO₃/Bi₂MoO₆ composite (Fig. 5B), however,

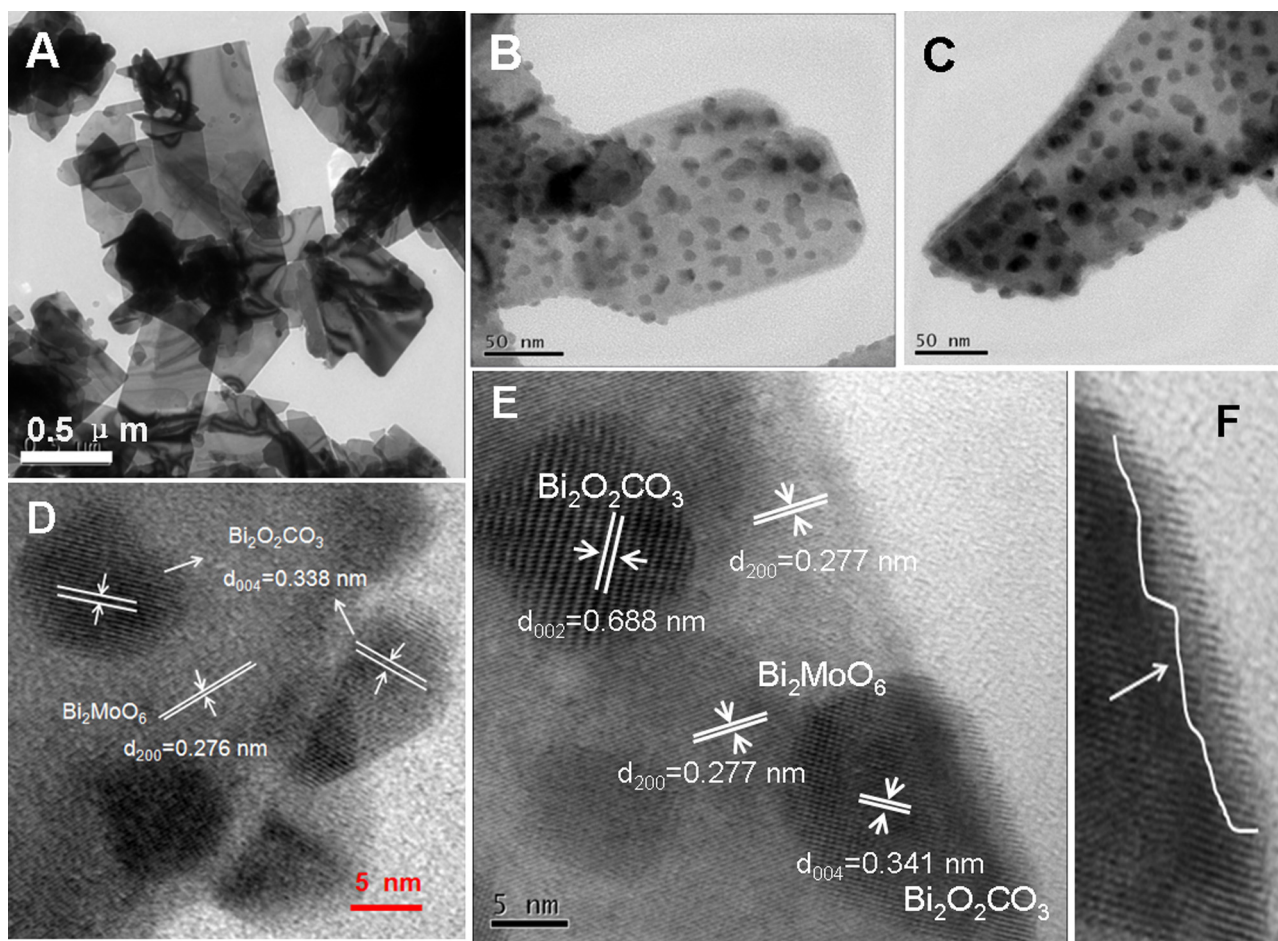
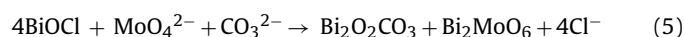
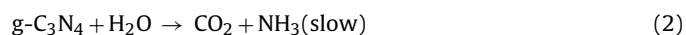
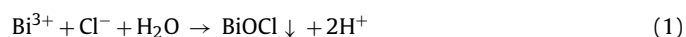


Fig. 4. TEM and HRTEM images of the $\text{Bi}_2\text{O}_2\text{CO}_3/\text{Bi}_2\text{MoO}_6$ composite.

shows new diffraction rings besides the strong diffraction spots of Bi_2MoO_6 . As revealed by the white and red rings in Fig. 5B, it can be measured that the lattice spacings are 0.294 and 0.199 nm, which are consistent with the distance between (013) and (020) planes of $\text{Bi}_2\text{O}_2\text{CO}_3$, respectively. This result further confirms the heterojunction of $\text{Bi}_2\text{O}_2\text{CO}_3$ and Bi_2MoO_6 .

3.2. Formation mechanism

The preparation strategy of this study is to use the BiOCl platelets as templates to chemically transform into $\text{Bi}_2\text{O}_2\text{CO}_3$ and Bi_2MoO_6 . In addition, it is found that the g- C_3N_4 , like mesoporous silica SBA-15, suffers from collapse of its structure in liquid water at high temperature [35]. Under the hydrothermal treatment, g- C_3N_4 decomposed to generate NH_4^+ and CO_3^{2-} . The resulted CO_3^{2-} exchanged with the Cl^- in BiOCl to form the $\text{Bi}_2\text{O}_2\text{CO}_3$. Based on the experimental results of the evolution of morphology and structure, a possible formation process of such heterostructured $\text{Bi}_2\text{O}_2\text{CO}_3/\text{Bi}_2\text{MoO}_6$ nanoplatelets has been schematically illustrated by an anion exchange and Ostwald ripening process. Accordingly, a chemical transformation process can be expressed by the following chemical reaction equations:



The plausible conversion from BiOCl to $\text{Bi}_2\text{O}_2\text{CO}_3/\text{Bi}_2\text{MoO}_6$ was achieved by anion exchange, as indicated in Scheme 1. With the same Aurivillius-type structure, BiOCl , $\text{Bi}_2\text{O}_2\text{CO}_3$ and Bi_2MoO_6 are crystallized in layered structures composed of $[\text{Bi}_2\text{O}_2]^{2+}$ slabs interleaved with anion layers, providing the possible transfer conditions from BiOCl to $\text{Bi}_2\text{O}_2\text{CO}_3/\text{Bi}_2\text{MoO}_6$ composite. Because the stability of $\text{Bi}_2\text{O}_2\text{CO}_3$ and Bi_2MoO_6 is higher than that of BiOCl , the transformation of BiOCl to $\text{Bi}_2\text{O}_2\text{CO}_3$ and Bi_2MoO_6 in the presence of CO_3^{2-} and MoO_4^{2-} is thermodynamically favored. This is similar to the formation of Bi_2WO_6 hollow microspheres by an anion exchange strategy based on Kirkendall effect [36]. The crystal structure models of BiOCl , $\text{Bi}_2\text{O}_2\text{CO}_3$, Bi_2MoO_6 and the corresponding composites are illustrated in Scheme 1. (I) is pure BiOCl crystal model. (II) and (III) represent BiOCl crystal partly replaced by MoO_4^{2-} . (IV) corresponds to the $\text{Bi}_2\text{O}_2\text{CO}_3/\text{Bi}_2\text{MoO}_6$ composite, in which the Cl^- in BiOCl crystal was fully replaced by CO_3^{2-} and MoO_4^{2-} . In such models, the interface dipole and the associated discontinuity in the local band structure at the interface are not considered, which always exist in semiconductor heterojunctions [31].

3.3. Photocatalytic activity of the $\text{Bi}_2\text{O}_2\text{CO}_3/\text{Bi}_2\text{MoO}_6$ nanocomposites

The degradation of RhB catalyzed by the $\text{Bi}_2\text{O}_2\text{CO}_3/\text{Bi}_2\text{MoO}_6$ composites under visible light was investigated to evaluate their

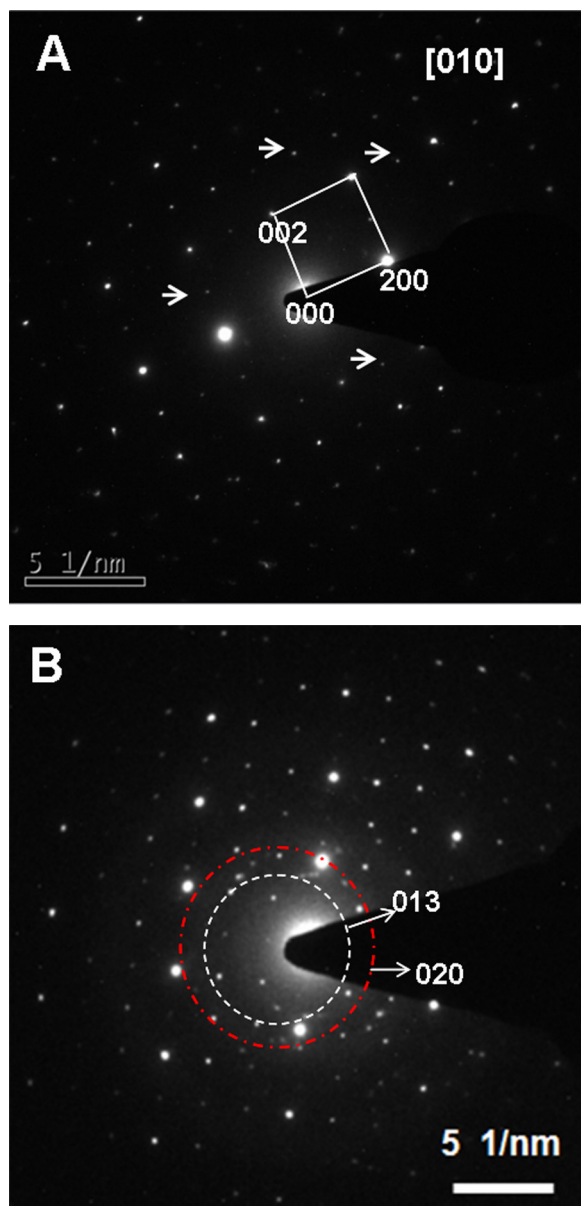


Fig. 5. The selected area electron diffraction images of the $\text{Bi}_2\text{O}_2\text{CO}_3/\text{Bi}_2\text{MoO}_6$ nanoplatelets, (A) for Bi_2MoO_6 and (B) for $\text{Bi}_2\text{O}_2\text{CO}_3/\text{Bi}_2\text{MoO}_6$ junction.

performance. As depicted in Fig. 6A, the photocatalytic activity of the $\text{Bi}_2\text{O}_2\text{CO}_3/\text{Bi}_2\text{MoO}_6$ nanoplatelets was higher than that of the bare $\text{Bi}_2\text{O}_2\text{CO}_3$ and Bi_2MoO_6 nanoplatelets. Blank test (without any catalyst) under visible light exhibited no photolysis of RhB. The degradation of RhB over $\text{Bi}_2\text{O}_2\text{CO}_3$ and commercial TiO_2 powders (P25) was almost inactive under visible light irradiation. Surprisingly, more than 99% of RhB was removed by the $\text{Bi}_2\text{O}_2\text{CO}_3/\text{Bi}_2\text{MoO}_6$ composite within 30 min. Furthermore, the adsorption and desorption equilibrium between catalyst and dye was established within 10 min in the dark. To clarify the primary cause for the superiorly enhanced photocatalytic activity of $\text{Bi}_2\text{O}_2\text{CO}_3/\text{Bi}_2\text{MoO}_6$ nanoplatelets, batch experiments were devised by varying the parameters which affect the growth process of the $\text{Bi}_2\text{O}_2\text{CO}_3/\text{Bi}_2\text{MoO}_6$, such as the synthesis temperature, the content of $\text{g-C}_3\text{N}_4$, the reaction time and medium.

Temperature exerts great impact on the formation of $\text{Bi}_2\text{O}_2\text{CO}_3/\text{Bi}_2\text{MoO}_6$ crystals, thus on the catalytic performance. As exhibited in Fig. S4, BiOCl was still found in the sample after

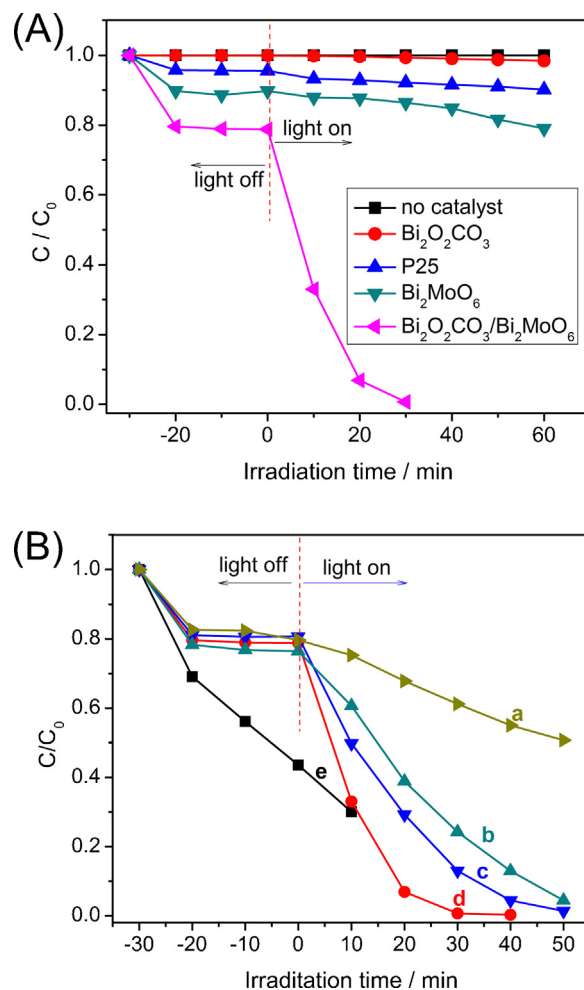


Fig. 6. Photocatalytic degradation of RhB (5.0 mg/L) over (A) various catalysts, and (B) Bi_2MoO_6 -based photocatalysts prepared at different reaction temperatures, (a) is pure Bi_2MoO_6 obtained at 180°C ; (b), (c), (d) are $\text{Bi}_2\text{O}_2\text{CO}_3/\text{Bi}_2\text{MoO}_6$ prepared at 160, 180, 200°C , respectively and (e) is $\text{BiOCl}/\text{Bi}_2\text{O}_2\text{CO}_3/\text{Bi}_2\text{MoO}_6$ obtained at 150°C .

hydrothermal reaction in the presence of Na_2MoO_4 and $\text{g-C}_3\text{N}_4$ at 150°C for 12 h (Fig. S4a). As the temperature increased to 180°C or above, only $\text{Bi}_2\text{O}_2\text{CO}_3$ and Bi_2MoO_6 were found based on the XRD result. As indicated by the structure characterization, the Bi_2MoO_6 is also enclosed by dominant (0 1 0) facets, confirming that an oriented growth occur with prolonging the reaction time (Fig. S4b) or increasing the temperature (Fig. S4c). In addition, the platelets of the $\text{Bi}_2\text{O}_2\text{CO}_3/\text{Bi}_2\text{MoO}_6$ become thicker upon the increase of temperature, as shown in Fig. S5. Moreover, it is found that the efficiency on the degradation of RhB by the prepared samples under visible light was quite different. As depicted in Fig. 6B, increasing the temperature for the preparation of the catalysts will decrease their photooxidation activity. The highest photocatalytic activity occurred over the catalyst prepared at 180°C (Fig. 6d). An extraordinary activity of the $\text{Bi}_2\text{O}_2\text{CO}_3/\text{Bi}_2\text{MoO}_6$ catalysts was observed with the catalyst being synthesized at 150°C , which can be ascribed to the photo-sensitization of BiOCl in the $\text{BiOCl}/\text{Bi}_2\text{O}_2\text{CO}_3/\text{Bi}_2\text{MoO}_6$ catalyst (Figs. 6e and S4a).

Apart from the reaction temperature, both the amount of $\text{g-C}_3\text{N}_4$ and reaction time have great effect on the primary growth of $\text{Bi}_2\text{O}_2\text{CO}_3/\text{Bi}_2\text{MoO}_6$. To verify the role of $\text{g-C}_3\text{N}_4$ amount and reaction time in the formation of $\text{Bi}_2\text{O}_2\text{CO}_3/\text{Bi}_2\text{MoO}_6$ as well as the related photocatalytic performance, control experiments were carried out. Notably, the apparent rate constant (k) in degradation of

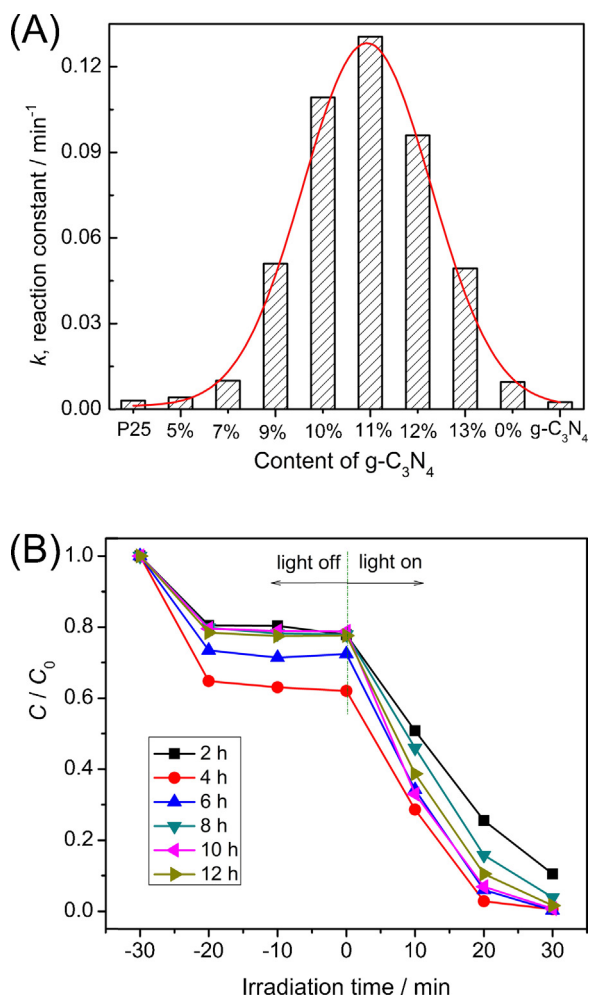


Fig. 7. (A) The degradation rate of RhB over Bi₂MoO₆-based photocatalysts starting from different amounts of g-C₃N₄; (B) photocatalytic degradation of RhB (5.0 mg/L) over the Bi₂MoO₆-based photocatalysts obtained in different reaction time.

RhB over the Bi₂MoO₆-based photocatalysts, as shown in Fig. 7A, increases remarkably with more g-C₃N₄. The rate summit reached at the 11 wt% g-C₃N₄ (the molar ratio of Bi₂O₂CO₃ to Bi₂MoO₆ is 18.8%, as illustrated in Table S1) with k of 0.1305 min⁻¹, which is about 64 times of pure Bi₂MoO₆ (0.0202 min⁻¹) (Fig. S6). P25 and Bi₂O₂CO₃ show almost no visible light activity, with the k of 0.003 min⁻¹ and 0.000314 min⁻¹, respectively. As aforementioned, the Bi₂O₂CO₃/Bi₂MoO₆ nanoplatelets were obtained instead of BiOCl/Bi₂MoO₆ nanoplatelets when the reaction time increased to 8 h in the presence of g-C₃N₄ (Fig. 2). The Bi₂O₂CO₃/Bi₂MoO₆ nanoplatelets prepared by hydrothermal treatment for 10 h show the highest photocatalytic activity (Fig. 7B). Further extension of the reaction time for the preparation of the catalysts does not increase their photocatalytic activity obviously. Furthermore, at given time, only platelet-like nanostructures were observed in the SEM images even if we start from different contents of g-C₃N₄ (Fig. S7). HRTEM provides insight into the secret of the different photocatalytic activity of the catalysts. As displayed in Fig. 8, although varying the amount of g-C₃N₄ in the starting reaction system allows little change of morphology, fewer nanoparticles of Bi₂O₂CO₃ in the Bi₂O₂CO₃/Bi₂MoO₆ composite were observed when smaller amounts of g-C₃N₄ were used (Fig. 8A and B). Moreover, the main component in the composite is Bi₂MoO₆ nanoplatelets with exposure of the (200) facet, which can be clearly found in the inset of the corresponding SAED pattern (Fig. 8C). By comparing

Figs. 4 and 8A, the platelet-structured Bi₂O₂CO₃/Bi₂MoO₆ becomes thicker as the g-C₃N₄ increased to 15 wt%, as presented in Fig. 8D and E. Obviously, plenty of Bi₂O₂CO₃ nanoparticles distributed in/on the whole Bi₂MoO₆ nanoplatelet. Fig. 8F further illustrates that the Bi₂O₂CO₃/Bi₂MoO₆ nanoplatelets are composed of several thinner layers, as indicated by the white arrows. Moreover, many Bi₂O₂CO₃ nanoparticles linked together, which leads to the loss of the interface between Bi₂O₂CO₃ and Bi₂MoO₆ and further deteriorates its catalytic activity. These observations demonstrate that the content of Bi₂O₂CO₃ in the composite plays a pivotal role in the photocatalytic activity. More importantly, the ratio of Bi₂O₂CO₃ in the composite catalysts can be successfully regulated in a sophisticated manner by altering the amount of g-C₃N₄ in the starting materials, thus optimize the catalysts for high performance.

In addition, the surface area is an important factor for the enhanced photocatalytic activity [37]. The Bi₂MoO₆-based platelet-like nanomaterials possess different surface areas, as evidenced by the nitrogen absorption experiment. The surface areas of the Bi₂O₂CO₃/Bi₂MoO₆ platelets increase from 3.3 m² g⁻¹ to 14.8 m² g⁻¹ upon the increase of g-C₃N₄ from 5 wt% to 11 wt%, respectively. However, more g-C₃N₄ leads to the decrease of surface area to 5.8 m² g⁻¹ (15 wt%). Another important consideration for such dramatic activity enhancement is the unique nanoplatelet junction with well-distributed Bi₂O₂CO₃ nanoparticles. The nanoplatelet morphology, as illustrated in Figs. 3D and 4A, helps to increase the surface area and shortens the distance for the transfer of photogenerated electrons from the interior to the surface, thus promotes the efficiency of the electron-hole separation and allowing more efficient use of the light and therefore offering an improved catalytic activity. More importantly, the heterostructures are very sensitive to reconstruction at the interface. The electronic orbitals of the atoms become partially occupied and the electrons can move between the two oxides ("electronic reconstruction"), that is, they are deformed from the normal shape so that the electronic structures of the two different oxides are blended [38]. Apart from that, the "lattice reconstruction" (the changes of the carrier density) [39] can also form because interfacial atoms are subject to forces different from those in bulk, leading to the position change of the atoms [40]. In this case, the lattice, electronic, and orbital reconstructions at the interface relative to the bulk are the origin of the exotic properties [38,41]. In the current Bi₂O₂CO₃/Bi₂MoO₆ heterostructures, the Bi₂O₂CO₃ nanoparticles are homogeneously scattered and embedded in Bi₂MoO₆ nanoplatelet matrix, forming large hetero-interfaces, as shown in Fig. 4, which can highly effectively maximize charge separation and minimize the recombination of carriers and correspondingly present a superior photocatalytic performance [42]. This suggests that the presence of the heterojunction, the exposure of both phases on the surface and the special sesame-biscuit-like structure are essential for the enhancement of photocatalytic activity of the catalysts.

3.4. Photocatalytic mechanism

In order to further reveal the high performance of the photocatalysts, UV-vis diffuse reflectance spectra (DRS) were recorded to verify the light harvesting ability of the synthesized Bi₂MoO₆-based composites. It can be clearly observed from Fig. S8, that the reaction temperature plays a particularly important role in the formation of the Bi₂MoO₆-based composites. In other words, the reaction temperature is the key to the anions exchange.

The top of the valance band (VB) and the bottom of the conduction band (CB) of Bi₂MoO₆ are calculated to be 2.41 V and -0.35 V, respectively, while the VB and CB of Bi₂O₂CO₃ are estimated to

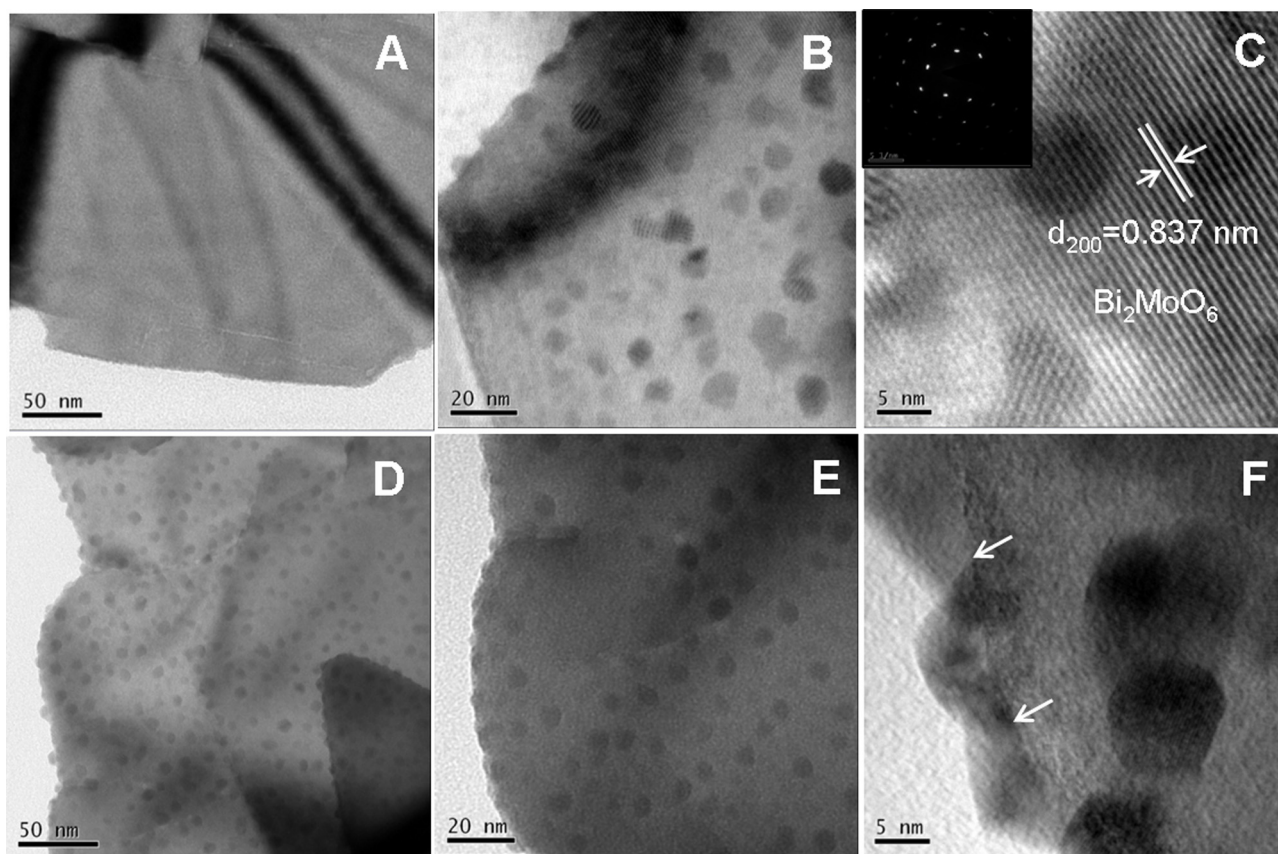
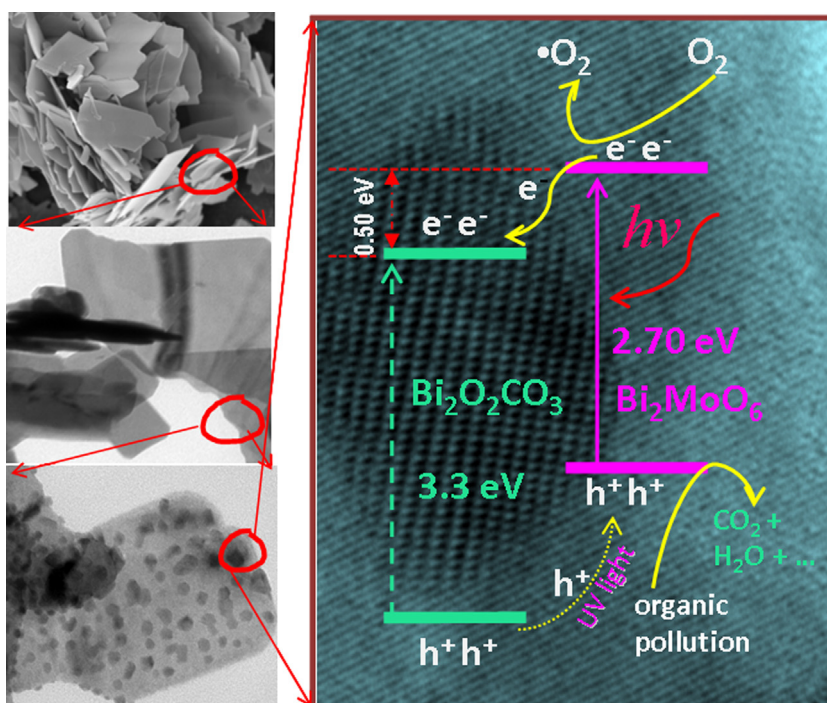


Fig. 8. TEM and HRTEM images of the $\text{Bi}_2\text{O}_2\text{CO}_3/\text{Bi}_2\text{MoO}_6$ composites prepared with different amounts of g- C_3N_4 , (A–C) 5 wt% g- C_3N_4 , (D–F) 15 wt% g- C_3N_4 .

be 3.51 V and 0.21 V, respectively, by means of Mulliken electronegativity theory (Fig. S8) [43]. Thus, the photogenerated electrons from Bi_2MoO_6 can reduce the surface chemisorbed O_2 to give $\cdot\text{O}_2^-$, through one-electron reaction ($\text{O}_2 + e^- \rightarrow \cdot\text{O}_2^-$,

$E(\text{O}_2/\cdot\text{O}_2^-) = -0.33 \text{ V vs. NHE}$) [44]. The photogenerated holes can oxidize OH^- to give $\cdot\text{OH}$ ($E(\text{OH}^-/\cdot\text{OH}) = 2.38 \text{ V vs. NHE}$). Therefore, it is possible that hole and $\cdot\text{OH}$ serve as the main active species involved in the photodegradation of organic compounds



Scheme 2. Schematic diagram of the energy band structure of the $\text{Bi}_2\text{O}_2\text{CO}_3/\text{Bi}_2\text{MoO}_6$ nanojunction and the possible charge transfer process under visible light irradiation.

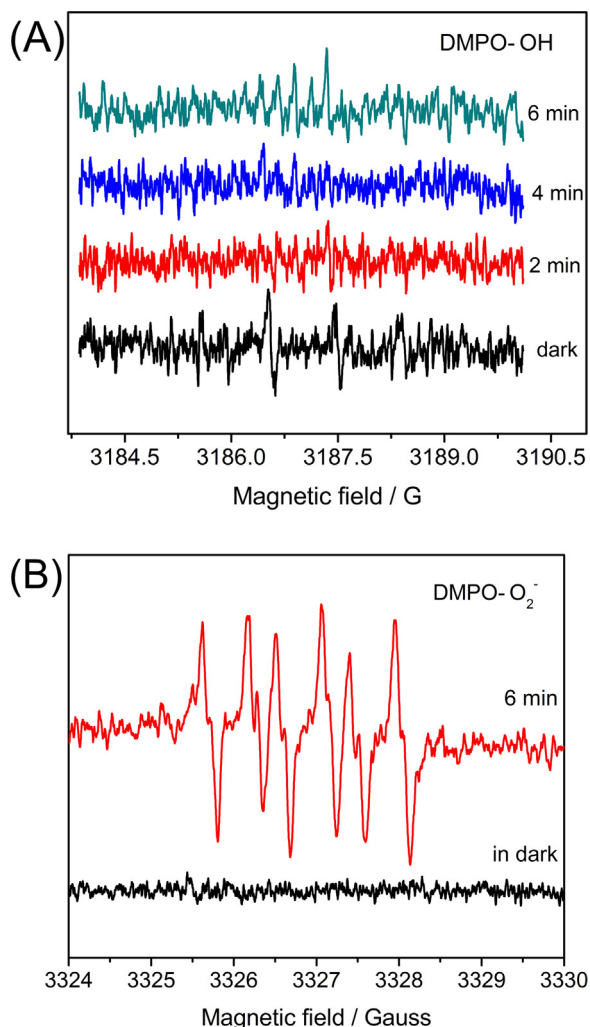


Fig. 9. DMPO spin-trapping ESR spectra recorded at ambient temperature in aqueous Bi₂O₂CO₃/Bi₂MoO₆ dispersion for DMPO-•OH (A), as well as in CH₃OH dispersion for DMPO-•O₂⁻ (B) under visible irradiation ($\lambda > 420$ nm). The settings for the ESR spectrometer were as follows: center field, 3367 G; sweep width, 80 G; microwave frequency, 9.44 GHz; modulation frequency, 100 kHz and power, 0.998 mW.

in the Bi₂O₂CO₃/Bi₂MoO₆ heterostructure. Electron spin resonance (ESR) spectroscopy with 5,5-dimethyl-1-pyrroline-N-oxide (DMPO) spin-trapping adducts allows the detection of hydroxyl radicals (DMPO-•OH) and superoxide radicals (DMPO-•O₂⁻). Consequently, ESR spin-trapping analysis was employed to probe the nature of the reactive species generated during irradiation of the present system. As shown in Fig. 9A, no signal of •OH was detected in the system containing Bi₂O₂CO₃/Bi₂MoO₆ under visible light irradiation, which suggests that direct hole oxidation is not the main reaction during photocatalytic process. As indicated in Fig. 9B, six apparent signals were generated, which were attributed to DMPO-•O₂⁻ with the Bi₂O₂CO₃/Bi₂MoO₆ in methanol under visible light irradiation for 6 min, while no •O₂⁻ signal was detected in dark under otherwise identical conditions [45]. N₂ purging experiment indirectly reflects the fact that •O₂⁻ is one kind of main oxidative species in the photocatalytic process, as indicated in Fig. S9. Under visible light irradiation, the photodegradation of RhB is obviously inhibited by the addition of the hole scavenger, disodiummethylenediamine tetraacetate (EDTA-2Na), the activity decreases down to 90% while it is slightly suppressed when the hydroxyl radical scavenger, tert-butyl alcohol or isopropanol, was added. This indicates that holes are the dominant active species that can oxidize the adsorbed organic pollutants. Based on the

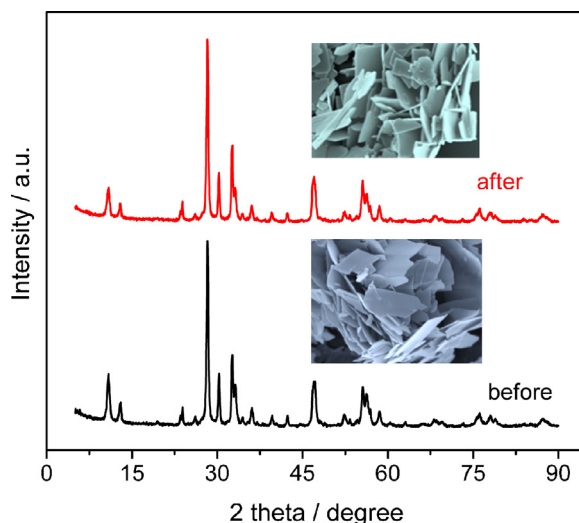


Fig. 10. XRD patterns and SEM images of the Bi₂O₂CO₃/Bi₂MoO₆ composites before and after the photocatalytic reaction.

above results, the photocatalytic process is mainly governed by the superoxide radical and the holes rather than the hydroxyl radicals.

The enhanced performance of the composite catalysts can be ascribed to the charge transfer process of the heterojunctioned Bi₂O₂CO₃/Bi₂MoO₆ nanoplatelets, as illustrated in Scheme 2. Although it cannot be excited by the visible light for degradation of organic pollution, Bi₂O₂CO₃ can accept the photo-generated electrons produced in Bi₂MoO₆ because it has more positive CB (+0.20 V), confirming that the photo-generated electrons and holes can be separated effectively, and the possibility of the recombination of electron-hole pairs decreases. Correspondingly, the holes can facilitate transfer and react directly with the absorbed RhB. Furthermore, the well-crystallized nanoplatelet texture is favorable for shortening the distance that electrons and holes transferred from bulk to the surface of the catalyst to participate in surface reactions [25], thus promoting the photocatalytic activity. All of the abovementioned resulted in the remarkably enhanced photocatalytic activity.

In addition, the Bi₂O₂CO₃/Bi₂MoO₆ composite was highly stable during the reaction and can be used repeatedly. The ICP-AES analysis showed that the leaching Bi³⁺ from the catalyst in the reaction solution was 0.047% after 6 h light illumination, which is negligible. After being reused for three times, as shown in Figs. 10 and S10, the photocatalytic activity of the Bi₂O₂CO₃/Bi₂MoO₆ nanoplatelets was almost unchanged. The SEM images and XRD patterns of the Bi₂O₂CO₃/Bi₂MoO₆ catalyst before and after catalytic reaction further demonstrate that the morphology and structure of the Bi₂O₂CO₃/Bi₂MoO₆ nanoplatelets remain intact. Furthermore, the nanoplatelets can be easily separated by a simple sediment process, which is advantageous for practical applications.

4. Conclusions

In summary, heterostructured sesame-biscuit-like Bi₂O₂CO₃/Bi₂MoO₆ nanoplatelets with adjustable content of Bi₂O₂CO₃ were successfully prepared by a facile anion exchange method under hydrothermal treatment. Compared to the pure Bi₂MoO₆ and Bi₂O₂CO₃, heterojunctioned Bi₂O₂CO₃/Bi₂MoO₆ nanoplatelets show dramatically enhanced visible light photocatalytic activity, and the as-prepared nanoplatelets exhibit a 64-fold faster rate than the single Bi₂MoO₆ nanoparticles. The heterojunction in the regions between Bi₂O₂CO₃ and Bi₂MoO₆ improved the

charge separation and consequently enhanced the efficiency of the degradation of RhB. Additionally, the photo-generated h^+_{VB} and $\bullet O_2^-$ in the $Bi_2O_2CO_3/Bi_2MoO_6$ photocatalysts turn out to be the leading active species in the photocatalytic reaction. This strategy can be further extended to the synthesis and study of new $Bi_2O_2CO_3$ -based nanostructures for environment and energy application.

Acknowledgments

Financial support of the work by the National Natural Science Foundation of China under Grant 21273080 and Guangdong Natural Science Foundation under Grant S2012010008383 is greatly acknowledged. The authors thank Prof. Yi-Ping Hang for assistance in the ICP-AES testing.

Appendix A. Supplementary data

Supplementary data associated with this article can be found, in the online version, at <http://dx.doi.org/10.1016/j.apcatb.2013.04.019>.

References

- [1] P.D. Yang, J.M. Tarascon, *Nature Materials* 11 (2012) 560–563.
- [2] X.X. Xu, C. Randorn, P. Efstathiou, J.T.S. Irvine, *Nature Materials* 11 (2012) 595–598.
- [3] A. Paracchino, V. Laporte, K. Sivula, M. Gratzel, E. Thimsen, *Nature Materials* 10 (2011) 456–461.
- [4] Z.G. Zou, J.H. Ye, K. Sayama, H. Arakawa, *Nature* 414 (2001) 625–627.
- [5] Z.G. Yi, J.H. Ye, N. Kikugawa, T. Kako, S.X. Ouyang, H. Stuart-Williams, H. Yang, J.Y. Cao, W.J. Luo, Z.S. Li, Y. Liu, R.L. Withers, *Nature Materials* 9 (2010) 559–564.
- [6] X.C. Wang, K. Maeda, A. Thomas, K. Takanabe, G. Xin, J.M. Carlsson, K. Domen, M. Antonietti, *Nature Materials* 8 (2009) 76–80.
- [7] Q.J. Ruan, W.D. Zhang, *Journal of Physical Chemistry C* 113 (2009) 4168–4173.
- [8] X. Xiao, W.D. Zhang, *Journal of Materials Chemistry* 20 (2010) 5866–5870.
- [9] Q.X. Jia, K. Iwashina, A. Kudo, *Proceedings of the National Academy of Sciences of the United States of America* 109 (2012) 11564–11569.
- [10] L.W. Zhang, C. Baumanis, L. Robben, T. Kandiel, D. Bahnemann, *Small* 7 (2011) 2714–2720.
- [11] L.Q. Ye, L. Zan, L.H. Tian, T.Y. Peng, J.J. Zhang, *Chemical Communications* 47 (2011) 6951–6953.
- [12] Y. Zheng, F. Duan, M.Q. Chen, Y. Xie, *Journal of Molecular Catalysis A: Chemical* 317 (2010) 34–40.
- [13] R. Chen, M.H. So, J. Yang, F. Deng, C.M. Che, H.Z. Sun, *Chemical Communications* 21 (2006) 2265–2267.
- [14] M. Shang, W.Z. Wang, J. Ren, S.M. Sun, L. Zhang, *Nanoscale* 3 (2011) 1474–1476.
- [15] L. Zhu, W.D. Zhang, C.H. Chen, B. Xu, M.F. Hou, *Journal of Nanoscience and Nanotechnology* 11 (2011) 4948–4956.
- [16] M.S. Gui, W.D. Zhang, *Nanotechnology* 22 (2011) 265601–265609.
- [17] O. Khaselev, J.A. Turner, *Science* 280 (1998) 425–427.
- [18] S.Y. Reece, J.A. Hamel, K. Sung, T.D. Jarvi, A.J. Esswein, J.J.H. Pijpers, D.G. Nocera, *Science* 334 (2011) 645–648.
- [19] Y.Y. Liu, W.J. Son, J.B. Lu, B.B. Huang, Y. Dai, M.H. Whangbo, *Chemistry – A European Journal* 17 (2011) 9342–9349.
- [20] T.B. Li, G. Chen, C. Zhou, Z.Y. Shen, R.C. Jin, J.X. Sun, *Dalton Transactions* 40 (2011) 6751–6758.
- [21] L. Chen, S.F. Yin, S.L. Luo, R. Huang, Q. Zhang, T. Hong, P.C.T. Au, *Industrial and Engineering Chemistry Research* 51 (2012) 6760–6768.
- [22] N. Li, L. Zhu, W.D. Zhang, Y.X. Yu, W.H. Zhang, M.F. Hou, *Journal of Alloys and Compounds* 509 (2011) 9770–9775.
- [23] Y.S. Xu, W.D. Zhang, *Dalton Transactions* 42 (2013) 1094–1101.
- [24] W.D. Zhang, L. Zhu, *Journal of Nanoscience and Nanotechnology* 12 (2012) 6294–6300.
- [25] L.A. Zhou, M.M. Yu, J. Yang, Y.H. Wang, C.Z. Yu, *Journal of Physical Chemistry C* 114 (2010) 18812–18818.
- [26] J. Ren, W.Z. Wang, M. Shang, S.M. Sun, E.P. Gao, *ACS Applied Materials & Interfaces* 3 (2011) 2529–2533.
- [27] L.W. Zhang, Y. Man, Y.F. Zhu, *ACS Catalysis* 1 (2011) 841–848.
- [28] J. Chakhalian, A.J. Millis, J. Rondinelli, *Nature Materials* 11 (2012) 92–94.
- [29] A. Ohtomo, H.Y. Hwang, *Nature* 427 (2004) 423–426.
- [30] S.C. Yan, Z.S. Li, Z.G. Zou, *Langmuir* 25 (2009) 10397–10401.
- [31] W.A. Harrison, E.A. Kraut, J.R. Waldrop, R.W. Grant, *Physical Review B* 18 (1978) 4402–4410.
- [32] J. Jiang, K. Zhao, X.Y. Xiao, L.Z. Zhang, *Journal of the American Chemical Society* 134 (2012) 4473–4476.
- [33] D.H. Wang, G.Q. Gao, Y.W. Zhang, L.S. Zhou, A.W. Xu, W. Chen, *Nanoscale* 4 (2012) 7780–7785.
- [34] D.V. Bavykin, J.M. Friedrich, F.C. Walsh, *Advanced Materials* 18 (2006) 2807–2824.
- [35] Y.J. Pagan-Torres, J.M.R. Gallo, D. Wang, H.N. Pham, J.A. Libera, C.L. Marshall, J.W. Elam, A.K. Datye, J.A. Dumesic, *ACS Catalysis* 1 (2011) 1234–1245.
- [36] H.F. Cheng, B.B. Huang, Y.Y. Liu, Z.Y. Wang, X.Y. Qin, X.Y. Zhang, Y. Dai, *Chemical Communications* 48 (2012) 9729–9731.
- [37] L.S. Zhang, W.Z. Wang, L. Zhou, H.L. Xu, *Small* 3 (2007) 1618–1625.
- [38] E. Dagotto, *Science* 318 (2007) 1076–1077.
- [39] J. Mannhart, D.G. Schlom, *Science* 327 (2010) 1607–1611.
- [40] J. Chakhalian, J.W. Freeland, H.U. Haberman, G. Cristiani, G. Khaliullin, M. van Veenendaal, B. Keimer, *Science* 318 (2007) 1114–1117.
- [41] H.Y. Hwang, Y. Iwasa, M. Kawasaki, B. Keimer, N. Nagaosa, Y. Tokura, *Nature Materials* 11 (2012) 103–113.
- [42] H. Tada, T. Mitsui, T. Kiyonaga, T. Akita, K. Tanaka, *Nature Materials* 5 (2006) 782–786.
- [43] Y. Xu, M.A.A. Schoonen, *American Mineralogist* 85 (2000) 543–556.
- [44] J. Jiang, H. Li, L.Z. Zhang, *Chemistry – A European Journal* 18 (2012) 6360–6369.
- [45] L.S. Zhang, K.H. Wong, H.Y. Yip, C. Hu, J.C. Yu, C.Y. Chan, P.K. Wong, *Environmental Science and Technology* 44 (2010) 1392–1398.